

PREDICTING DROP DYNAMICS IN SUB-CRITICAL WEBER NUMBER REGIME: HIGH-FIDELITY SIMULATION AND DATA-DRIVEN MODELING

T. H. Mahmood¹, A. K. Tonmoy², C. Severt², Y. Wang², Y. Ling^{2,*}

¹Baylor University, Waco, TX
²University of South Carolina, Columbia, SC

ABSTRACT

Accurate prediction of the dynamics of a deformable and freely-moving drop in a uniform gas stream is essential for numerous applications involving droplets, such as spray cooling and liquid fuel injection. When the droplet Weber number is finite but moderate, the drop deviates from its spherical shape and deforms as it is accelerated by the gas stream. Since the drag depends on the drop shape, rigorously resolving the drop shape evolution is necessary for accurate predictions of the drop's velocity and position. In this study, 2D axisymmetric interface-resolved simulations were performed using the Basilisk solver. The sharp gas-liquid interface is resolved using a geometric Volume-of-Fluid (VOF) method. The quadtree mesh is used to discretize the 2D domain, providing flexibility to dynamically refine the mesh in user-defined regions. The adaptation criterion is based on the wavelet estimate of the discretization errors of the color function and all velocity components. Parametric simulations are conducted by systematically varying the Weber and Reynolds numbers. The instantaneous drop shapes are characterized using spherical harmonic modes. The temporal evolution of the drag and the spherical harmonic mode coefficients are investigated to identify correlations between the drag and the spherical harmonic mode coefficients. The simulation data are also utilized to develop point-particle models for Euler-Lagrange simulations of sprays consisting of a large number of drops. Due to the complex interplay between droplet drag and deformation, accurate models cannot be developed through conventional physics-based approaches. Therefore, a data-driven approach will be adopted. The spherical harmonic mode coefficients up to the sixth mode are used to characterize the drop shape. The evolutions of the spherical harmonic mode coefficients from the simulation results for cases in the test set are used to train the Non-linear Auto-Regressive with Exogenous input Neural Network (NARXNN) model. The predicted mode coefficients are then used as input to

train an additional NARXNN model for the drop acceleration.

Keywords: ASME conference paper, L^AT_EX Template, BibT_EX

NOMENCLATURE

a_c^*	Normalized acceleration
C_n	Coefficient of the n^{th} spherical harmonic mode
D_0	Initial drop diameter
L_x	Length of the liquid drop in axial direction
L_y	Length of the liquid drop in radial direction
Oh	Ohnesorge number
Re	Reynolds number
t_p	Number of timesteps predicted in each prediction step
U_0	Free stream velocity
We	Weber number
x	x co-ordinate
y	y co-ordinate
\mathbf{y}	Model output
μ_g	Viscosity of gas
μ_l	Viscosity of liquid
ρ_g	Density of gas
ρ_l	Density of liquid
σ	Surface tension
τ	Drop breakup time

1. INTRODUCTION

Accurate prediction of the dynamics of freely moving drops is important in many industrial application such as rain drop impact on aerodynamic surfaces, fuel-injection, and spray cooling [1]. In the present study, the dynamics of droplets are considered in a ideal situation, i.e, an isolated drop is suddenly exposed to a uniform gas stream, which has been widely used to study drop deformation and breakup [2, 3]. The morphological evolution and dynamics of drops are fully determined by the densities and viscosities of the drop liquid and the gas, ρ_l , μ_l , ρ_g , μ_g , the surface tension σ , the initial drop diameter D_0 , and the free-stream gas stream velocity U_0 . The subscripts g and l are used for variables associated with the gas and liquid, respectively, while the

*Corresponding author: stanley_ling@sc.edu
 Documentation for asmeconf.cls: Version 1.34, July 28, 2023.

subscript 0 represents the initial state. The present investigation is focused on the incompressible flow regime, in which the Mach number based on the relative velocity is always lower than 0.3, therefore, the compressibility effect on drop dynamics and deformation can be ignored.

In the present study, the liquid and gas properties are fixed: the drop liquid is water, and the gas is air. A parametric study will be performed by varying U_0 and D_0 . Previous observations [3, 5] have shown that $We = \rho_g U_0^2 D_0 / \sigma$ is the dominant dimensionless parameter governing the aerodynamic breakup for water drops. Due to the low viscosity of water, the Ohnesorge number $Oh = \mu_l / \sqrt{\rho_l D_0 \sigma}$ is generally small, unless for very small D_0 . Therefore, surface tension is more important than liquid viscosity as a force to resist drop deformation and breakup. Hence, the Weber and Reynolds numbers $Re = \rho_g U_0 D_0 / \mu_g$ are the most relevant parameters. If We is greater than a certain threshold, i.e., the critical Weber number We_{cr} , breakup will occur. Previous studies show that $We_{cr} \approx 11 \pm 2$ for drops with low Oh and high Re and liquid-to-gas density ratio $r = \rho_g / \rho_l$. Though the long-term research goal is to investigate the dynamics for the wide parametric space covering all breakup modes, the present study is focused on drops for which We is finite but lower than We_{cr} . Therefore, drops considered here will only undergo oscillation but will not break and form child droplets. Nevertheless, predicting the dynamics of drops in the sub- We_{cr} range is important for sprays and atomization simulations, as they comprise a significant portion of the population.

The significant deformation makes the interaction between the viscous gas flow around the drop deformation complicated. In the limit of $U_0 = 0$, the shape oscillations for stationary drops are purely driven by the capillary force. Analytical solutions are available for small-amplitude oscillations for inviscid drops [6] and viscous drops [7]. The viscous effect on free drop oscillation was further investigated in later studies [8–10]. As the drop interacts with the surrounding gas flows for finite We , the drop shape can deviate significantly from the initial spherical shape and can trigger a large-amplitude oscillation. Previous studies on the nonlinear effect due to large oscillation amplitude on the drop oscillation dynamics [11, 12] indicated that the drop oscillation frequency decreases when the oscillation amplitude increases. Furthermore, as the drop shape changes, the external gas flow and the liquid flow inside the drop can be significantly modulated [13–15]. As a result, the drag coefficient will also be different from the spherical counterpart. The modification of drag and the drop acceleration will, in turn, influence the interfacial instability and drop deformation.

In practical simulations of sprays consisting of a large number of droplets, it is impractical to resolve the interface of each individual drop. Instead, the drops are represented by Lagrangian point-particles [16–18]. The drop motion, shape deformation, topology change, and heat and mass transfer between the drop and the surrounding flow need to be captured by subgrid models [3, 19]. For drops with finite We , traditional force models for spherical drops [20] in the zero- We limit will be invalid. Though different physics-based models have been proposed [19, 21–23], significant discrepancies between the model predictions and high-fidelity simulation and experiment are observed. The funda-

mental challenge of physics-based models lies in the necessary assumptions/simplifications of the drop shape and surrounding flows, such as assuming the drop shape is a spheroid, which are typically valid only for a limited time period. Therefore, data-driven modeling is an important alternative. Data-driven models have been shown to be a powerful tool in multiphase flow research, such as predicting the trajectories of bubbles in turbulent flows at different Reynolds numbers [24], among many others [25–27]. However, to the authors' knowledge, data-driven models to predict droplet shape and drop dynamics remain to be established.

The goal of the present study is therefore to investigate the drop shape oscillation and acceleration in the sub-critical Weber number regime through high-fidelity interface-resolved simulations and to use the simulation data to develop data-driven models to predict the drop shape evolution and acceleration using Non-linear auto-regressive with exogenous input neural network (NARXNN).

2. METHODOLOGY

2.1 Simulation methods

The present simulations are conducted by the open-source, multiphase flow solver *Basilisk*. The incompressible Navier-Stokes equations with surface tension is solved using a finite-volume method for spatial discretization. The projection method is used to incorporate the incompressibility condition. Sharp interfaces separating the two phases are traced by solving the advection equation via a mass-momentum consistent geometrical Volume-of-fluid (VOF) method [28, 29]. The balanced-force method is used to discretize the singular surface tension term in the momentum equation [30]. The interface curvature required to calculate surface tension is computed based on the height-function (HF) method [30]. The staggered-in-time discretization of the volume fraction/density and pressure leads to a formally second-order-accurate time discretization [30]. An adaptive quadtree mesh is used to discretize the computational domain, which allows adaptive mesh refinement (AMR) in user-defined regions. The mesh adaptation is based on the wavelet estimate of the discretization errors of the liquid volume fraction and velocity [31]. A module was integrated into the *Basilisk* solver to extract the spherical harmonic mode coefficients during the simulation. The module to extract the mode coefficients were validated by testing predefined mode.

2.2 Physical parameters and simulation cases

The liquid and gas used in the present study are water and air at room temperature. The properties are listed in Table 1. The initial drop diameter and free-stream velocity are varied, resulting in a range of dimensionless parameters shown in Table 2. It can be seen that $Oh < 0.086$, indicating that the effect of liquid viscosity on drop breakup is generally small [5]. It is also affirmed that $M < 0.3$, so the compressibility effect can be ignored. Therefore, the current parametric study is focused on the effects of We and Re , and wide ranges of them are considered: $0.1 \leq We \leq 10$ and $10 \leq Re \leq 1000$. The boundaries of the regime of study are shown in Fig. 1(b). The two boundaries $Re = 1608We^{0.535}$ and $Re = 53.02We^{0.913}$ correspond to drops with $D_0 = 1$ cm

TABLE 1: FLUID PROPERTIES FOR SIMULATION CASES.

ρ_l (kg/m ³)	ρ_g (kg/m ³)	μ_l (Pa s)	μ_g (Pa s)	σ (N/m)
1000	1.2	0.001	0.000018	0.072

TABLE 2: RANGE OF DIMENSIONLESS PARAMETER FOR SIMULATION CASES.

We	Re	Oh	M
$\rho_g U_0^2 D_0 / \sigma$	$\rho_g U_0 D_0 / \mu_g$	$\mu_l / \sqrt{\rho_l D_0 \sigma}$	U_0 / C
0.1 – 10	10 – 1000	0.0012 – 0.0861	0.001 – 0.3

and $D_0 = 1 \mu\text{m}$, respectively. The present study is focused on the moderate-Re regime, so we have set the maximum Re to be 1000. Similarly, we have set the maximum We to be 10 to avoid drop breakup. A Latin Hypercube Sampling was performed over the Re-We parameter space of to investigate the drop behavior at different physical parameter combinations. A total of 102 cases were selected in the regime of interest (see Fig. 1(c)). For developing and testing the data-driven models, 92 and 10 cases were chosen as the training and testing sets, respectively. As will be discussed later in Section 3.4.1, the training data set will be further divided into four regions based on Re and We to improve model accuracy.

2.3 Simulation setup

A spherical drop is initially placed in a 2D-axisymmetric computational domain filled with stationary gas at $t = 0$. The setup is shown in Fig. 1(a). To make the investigation computationally feasible, we have opted for 2D-axisymmetric simulations for this study, which allows us to run 100 cases efficiently, whereas 3D simulations would be too expensive. At $t = 0^+$, a uniform velocity is applied to the left boundary of the domain, and a pressure outflow boundary condition is invoked on the right boundary. In an infinitesimal time (one time step in the simulation), the gas is suddenly accelerated to a velocity U_0 due to the incompressibility condition. The bottom of the domain serves as the axis, and the top is a slip wall. The domain is a square with an edge length of $l = 16D_0$, and the drop is initially placed at a distance of $x_0 = 2D_0$ away from the inlet.

To discretize the computational domain, we use quadtree mesh, which is dynamically adapted based on the wavelet estimates of the discretization errors of the liquid volume fraction and velocity components [31]. The minimum cell size Δ is controlled by the maximum refinement level \mathcal{L} , where $\Delta = l/2^{\mathcal{L}}$. For the results presented here, we have chosen $\mathcal{L} = 11$, corresponding to 128 minimum quadtree cells across the initial drop diameter, i.e., $N = D_0/\Delta = 128$. Further details on the grid-refinement study will be provided below to demonstrate that the mesh resolution is sufficient for the simulations.

3. RESULTS AND DISCUSSIONS

3.1 Validation and verification

To verify that the mesh is fine enough to resolve the oscillation dynamics, a grid-refinement study is performed. A drop with $D_0 = 1.55 \text{ mm}$ and $U_0 = 3.6 \text{ m/s}$, corresponding to $We = 0.33$ and $Re = 372.1$, is considered. For this low We, the drop shape

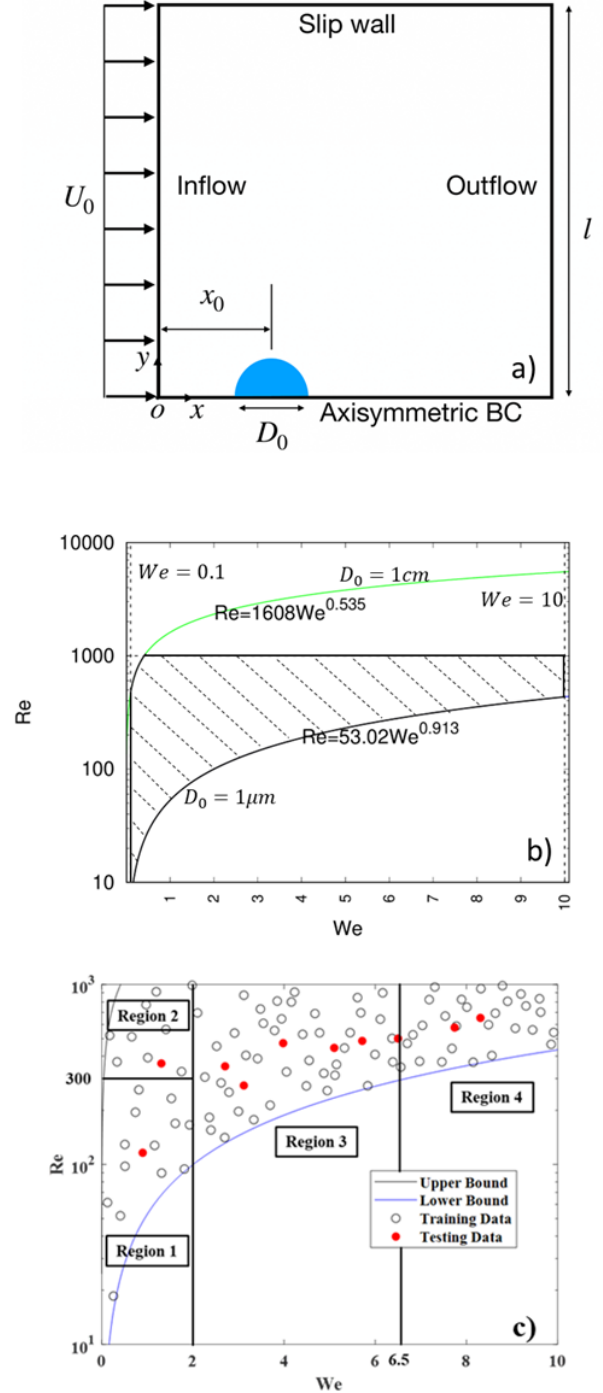


FIGURE 1: PARAMETER SPACE AS AN ARRAY OF WE AND RE CONFIRMING THE DROP SIZE BETWEEN $1 \mu\text{m} \leq D_0 \leq 1 \text{ cm}$ AND $M \leq 0.3$. HERE, WE NUMBER HAS BEEN TAKEN IN LINEAR SCALE AND THE RE IS IN LOGARITHMIC SCALE

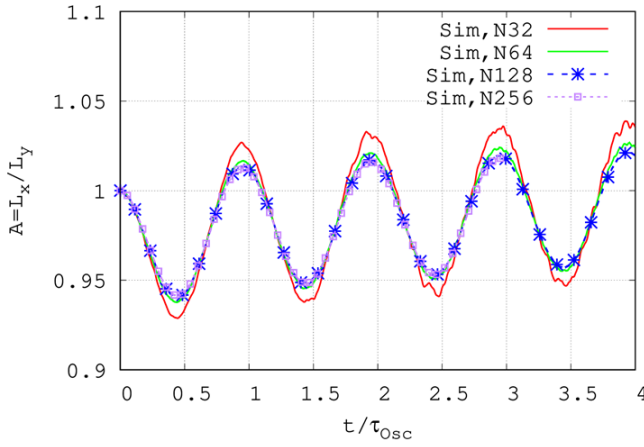


FIGURE 2: EVOLUTION OF THE ASPECT RATIO OF THE OSCILLATING DROP $\mathcal{A} = L_x/L_y$ OVER TIME FOR DIFFERENT MESH RESOLUTIONS $N = D_0/\Delta_{min} = 32, 64, 128$ AND 256 RESPECTIVELY.

oscillation is mainly controlled by surface tension, and it is expected the oscillation frequency will match with the Lamb frequency for the oscillation of a free drop. The aspect ratio of the drop, denoted as \mathcal{A} , is defined as the ratio of L_x to L_y , where L_x is the distance between the maximum and minimum positions on the drop surface along the x direction, and L_y is twice the maximum interfacial position in the y direction. The time-evolution of \mathcal{A} is plotted for different mesh levels, specifically, $\mathcal{L} = 9, 10, 11$, and 12 , corresponding to the number of cells across the initial drop diameter, $N = D_0/\Delta = 32, 64, 128$, and 256 , respectively (see Fig. 2). Time is normalized by $\tau_{osc} = \tau_{2,lamb}$ since the second mode is dominant. The Lamb frequency of the n^{th} axisymmetric spherical harmonic mode is given by [7]:

$$\omega_{n,lamb} = \sqrt{\frac{(n-1)n(n+1)(n+2)\sigma}{(n+1)\rho_l + n\rho_g}}. \quad (1)$$

From the results, it is evident that the N128 and N256 simulations overlap with each other, indicating mesh convergence at N128. Therefore, the N128 mesh is used for the rest of the simulations. Additionally, it is evident that the oscillation period is $t/\tau_{osc} = t/\tau_{lamb,2} = 1$, implying that the oscillation frequency obtained from the numerical simulation agrees well with the Lamb frequency for the second mode. This agreement validates the reliability of the present simulation methods.

3.2 Mode decomposition of spherical harmonic

The instantaneous drop shape is decomposed into spherical harmonic modes to characterize the drop morphological evolution. In the present study, only axisymmetric modes are considered, so in the cylindrical coordinate, the drop surface can be described as $R(\theta, t)$. In the small-amplitude limit, $R(\theta, t)$ can be represented as a linear combination of modes as

$$\frac{R(\theta, t) - R_{avg}}{R_{avg}} = \sum_{n=0}^{\infty} C_n(t) P_n(\cos(\theta)), \quad (2)$$

where P_n is the Legendre polynomial and C_n is the coefficient corresponding the spherical harmonic mode n . The first two

modes represents the volume and translation of the drop center, while modes for $n \geq 2$ represent the shape deviation from the initial spherical state. The values of C_n can be obtained by inverse transform from the instantaneous shape of the drop,

$$C_n(t) = \frac{2n+1}{2} \int_{-1}^1 \frac{R(\theta, t) - R_{avg}}{R_{avg}} P_n(\cos(\theta)) d(\cos(\theta)). \quad (3)$$

The mode coefficients are extracted from the simulation for every ten time steps. The x - y coordinates of the drop surface are first computed from the VOF reconstructed interface. Then taking the centroid as the origin of the spherical coordinate, the R - θ coordinates can be obtained, based on which the mode coefficients are calculated using Eq. (3). The temporal evolution of Fourier-Legendre coefficients for modes $n = 2 - 7$ and representative case are plotted in Fig. 3. All the mode coefficients are initially zero since the the drop is perfectly spherical at $t = 0$. As the drop is exposed to the incoming gas stream, it starts to deform and oscillate. It is shown that evolution of C_2 is similar to a sinusoid function, while the mean of C_2 oscillation increases with time.

3.3 Effect of finite oscillation amplitude

For small-amplitude oscillation, the drop shape can be accurately represented by a linear superposition of different spherical harmonic modes [7]. However, when the drop oscillation amplitude becomes finite, non-linear effects become significant [12, 32, 33]. The frequency spectra for the time evolutions of C_n are shown in Fig. 4, where nonlinear mode coupling can be identified [32]. While all the modes exhibit a primary frequency that matches well with the Lamb frequencies $\omega_{n,lamb}$, multiple secondary frequencies corresponding to other modes ω_m ($m \neq n$) are observed. Since the $n = 2$ mode is dominant, modes with $n > 2$ always show peaks at frequencies that correspond to the $n = 2$ mode, indicating energy transfer from higher-order modes to the dominant $n = 2$ mode. In general, the oscillation amplitude decreases with n , based on which we have truncated modes with $n \geq 10$.

Furthermore, when the drop deformation amplitude is finite, C_0 and C_1 will not be exactly equal to zero, as would be the case for small-amplitude oscillation of a stationary free drop. This is because the drop centroid will not be exactly the same as the center of the drop in its equilibrium shape. Due to a similar reason, C_0 does not exactly represent the drop volume, either.

3.4 Data-driven modeling approach

The present simulation results will be used to develop data-driven models for drop oscillation and acceleration. The models are based on the Non-linear Auto-Regressive with eXogenous input Neural Network (NARXNN). Two separate models will be built to predict the drop shape and acceleration (or drag), which are referred to as the *drop deformation model* and *drop acceleration model*, respectively. The drop deformation model will predict the time evolutions of the coefficients of the spherical harmonic modes, based on which the time-varying drop shapes can be reconstructed. The separate drop acceleration model will incorporate the predicted mode coefficients as inputs to predict the time evolution of the normalized acceleration, since the shape oscillation will influence the drag and the resulting drop acceleration. The flow chart for the two models is shown in Fig. 5.

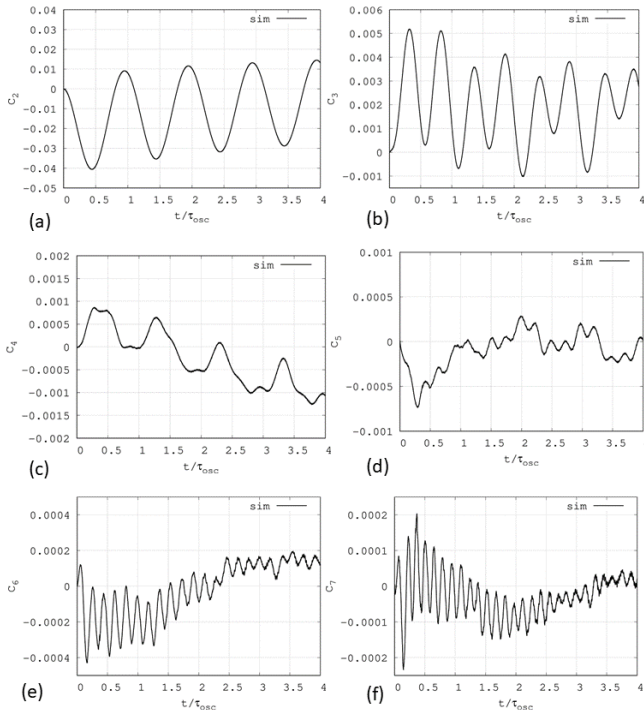


FIGURE 3: EVOLUTION MODE COEFFICIENTS OVER TIME.

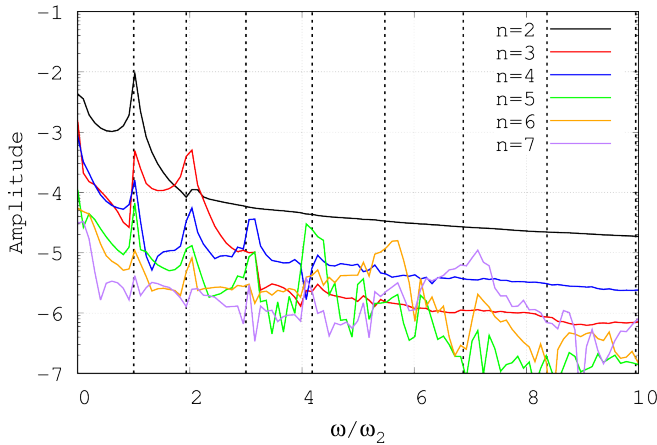


FIGURE 4: FREQUENCY SPECTRA OF FOURIER-LEGENDRE COEFFICIENTS INDICATING MODE COUPLING. THE RED MARKED SECTION IS ZOOMED IN FIGURE (B)

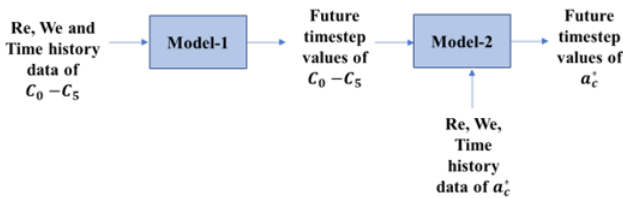


FIGURE 5: PROPOSED MODEL FLOWCHART

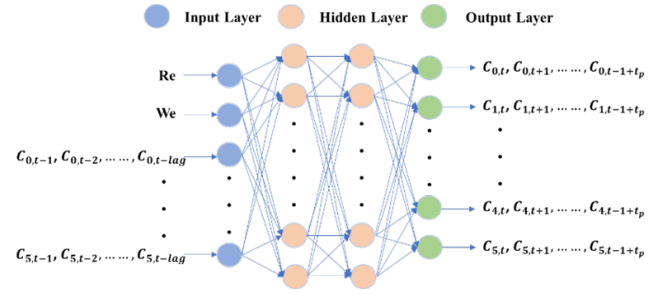


FIGURE 6: REPRESENTATION OF NARX MODEL ARCHITECTURE

3.4.1 Non-linear auto-regressive with exogenous input neural network (NARXNN) architecture. The Non-linear auto-regressive with exogenous input neural network (NARXNN) is a recurrent neural network (RNN) model that predicts the system's outputs as a nonlinear combination of previous outputs and inputs. This model has been proven to be accurate in modeling non-linear time-dependent systems [34]. In the present study, the exogenous inputs are the physical parameters (Re and We). The NARXNN model can be expressed as:

$$\mathbf{y}(t, t+1, \dots, t_p) = F[\mathbf{y}(t-1), \dots, \mathbf{y}(t-\text{lag}), Re, We] \quad (4)$$

where \mathbf{y} represents the outputs of the model, which will be the mode coefficients. The variables t_p and lag control the number of future time steps predicted and the number of previous time steps used in each prediction step, respectively. In this model, lag = 50 and $t_p = 10$, meaning that at each prediction step, the fifty previous time steps' data is used to predict the next ten time steps. A representative model architecture is shown in Fig. 6. A NARXNN model can be open-loop, where the previous outputs $\mathbf{y}(t-1, \dots, t-\text{lag})$ are known or measured, or closed-loop, where the predicted outputs are fed back as inputs. In the present NARXNN model, the training will be open-loop, utilizing the full simulation data as both input and output, while the evaluation will be closed-loop and utilize only the first lag time steps of simulation data.

To simplify the modeling, only the first six mode coefficients are used, though the simulation results for first ten modes are available. Therefore, to predict the droplet shape, the first six (6) mode coefficients ($C_0 - C_5$). The present model consists of five (5) hidden layers. The neurons in each layer are selected based on trial and error. To predict the drop acceleration, a_c^* , the time history data of a_c^* was added as input. Based on data analysis, it was found that there is a significant variation in the oscillation amplitudes of mode coefficients and acceleration across the parameter space. Furthermore, cases with higher We have shorter simulation time and therefore less training data. Both attributes make modeling the full parameter space difficult. This issue can be mitigated by dividing the parameter space is divided into four regions (see Fig. 1(c)) and develop separate models for each region. Such a modeling approach is used for both mode coefficients and drop acceleration. The drop acceleration is normalized as $a_c^* = a_c (\frac{D_0}{U_0^2})$. The time evolution of a_c^* for each simulation case in the four regions are presented in Fig. 7 and a summary of the four regions is given in Table 3. As evident, even with normalization, the different regions have vastly different characteristics

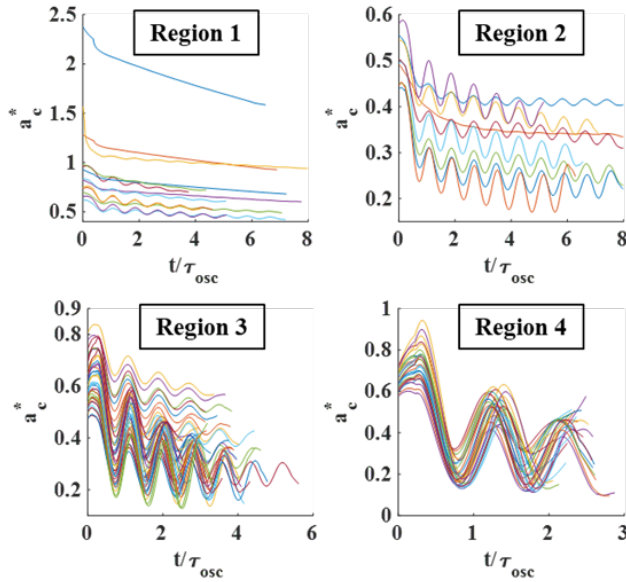


FIGURE 7: SEGMENTATION OF PARAMETER SPACE

and separate models are needed for different regions to achieve the best accuracy across the entire parameter space, unless better ways to normalize the data can be found. All the models will have the same architecture and hyperparameters but will be trained on different datasets.

The error metrics used to evaluate the model performance are absolute and relative errors, defined as

$$\text{Absolute Error} = y_{\text{pred}} - y_{\text{sim}} \quad (5)$$

$$\text{Relative Error} = \frac{y_{\text{pred}} - y_{\text{sim}}}{y_{\text{sim}}} \times 100\% \quad (6)$$

where $y = R(\theta)/R_{\text{avg}}$ and $y = a_c^*$ for the drop deformation and acceleration models, respectively. Both error for each Re-We combination is first averaged over time, and the time-averaged errors are then again averaged for all cases to get the final mean errors.

3.4.2 Model prediction for drop deformation. Figure 8 shows the prediction accuracy of the mode coefficients ($C_0 - C_5$) for a test case (Re = 274.8, We = 3.12) in Region 3. The predictions are in good agreement with the simulation results, however, as time increases the error propagates and slight errors can be identified at the end region. The present model accurately captures the frequency and amplitude of the time oscillation of the mode coefficients ($C_0 - C_5$). Figure 9 shows the droplet shapes reconstructed from the mode coefficients at different t/τ_{osc} . It is shown that the predictions agree very well with the simulation results.

Table 4 summarizes the errors of shape prediction of different regions. The maximum mean relative error is in the testing dataset of Region 4, which is below 3%. The significant difference between the errors of Region 4 and the other regions is attributable to the large deviations in droplet shape associated with the higher Re and We. Also, this region has greater dependence on the higher mode coefficients ($C_6 - C_{11}$) which are not included in model. Even

TABLE 3: SUMMARY OF REGIONS.

Region	Boundary	Training Point	Testing Point
Region 1	$0.1 \leq \text{We} \leq 2$ $10 \leq \text{Re} \leq 300$	13	1
Region 2	$0.1 \leq \text{We} \leq 2$ $300 \leq \text{Re} \leq 1000$	9	1
Region 3	$2 \leq \text{We} \leq 6.5$	42	6
Region 4	$6.5 \leq \text{We} \leq 10$	28	2

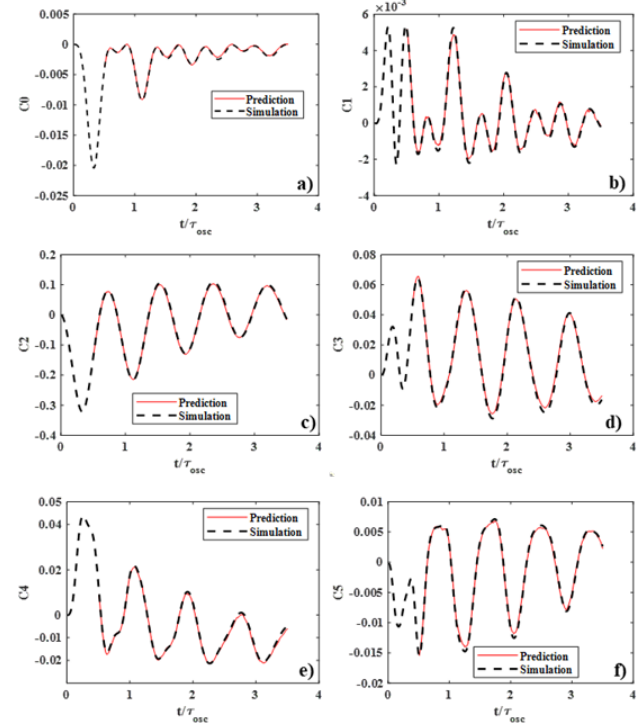


FIGURE 8: NARX PREDICTION AND HIGH FIDELITY SIMULATION RESULTS OF MODE COEFFICIENTS ($C_0 - C_5$) OVER TIME OF AN EXAMPLE TEST CASE (Re = 274.8, We = 3.12)

with these limitations, the largest relative error of any of the cases is 5.11%, which is associated with the Re = 900.04, We = 6.16 simulation case.

3.5 Prediction of the drop acceleration

With the shape prediction model validated, the mode coefficient predictions are now incorporated into the second model to predict the drop acceleration. Fig. 10 shows the prediction accuracy of a_c^* over time for different regions of the parameter space. Due to the drop shape oscillation, a_c^* also evolves in an oscillatory manner. For all four regions, the models capture the frequency and amplitude of a_c^* well but are less accurate in predicting the

TABLE 4: SUMMARY OF NARX RESULT FOR SHAPE PREDICTION.

Region	Relative Error		Absolute Error	
	Testing	Training	Testing	Training
Region 1	0.07	0.10	0.0006	0.0010
Region 2	0.28	0.26	0.0028	0.0026
Region 3	0.48	0.50	0.0047	0.0049
Region 4	2.67	2.21	0.0234	0.0179
Mean	0.79%	1.01%		

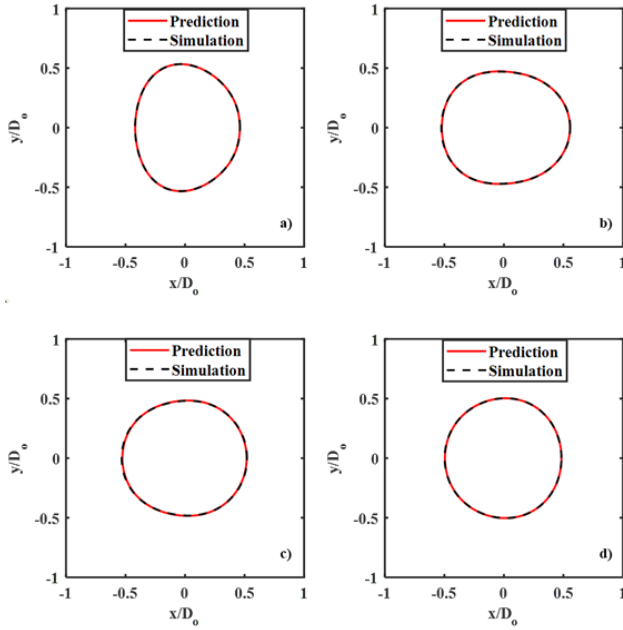


FIGURE 9: NARX PREDICTION AND HIGH FIDELITY SIMULATION RESULTS OF DROPLET SHAPE AT (A) $t/\tau_{osc} = 0.51$ (B) $t/\tau_{osc} = 1.5$ (C) $t/\tau_{osc} = 2.5$ AND (D) $t/\tau_{osc} = 3.5$ OF THE EXAMPLE TEST CASE ($Re = 274.8$, $We = 3.12$)

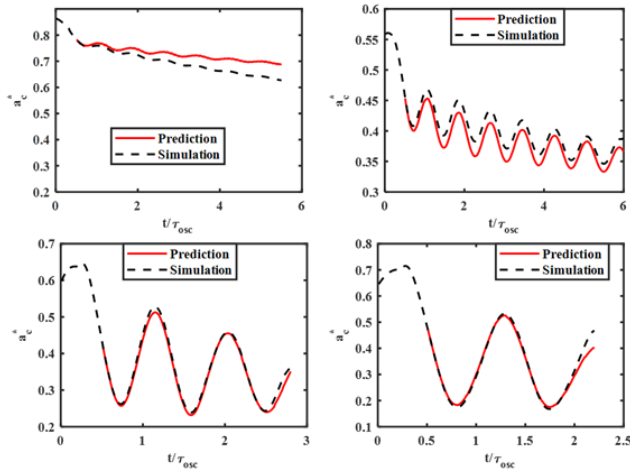


FIGURE 10: NARX PREDICTION AND HIGH FIDELITY SIMULATION RESULTS OF a_c^* FOR TEST CASE IN (A) REGION 1 ($Re = 116.13$, $We = 0.898$), (B) REGION 2 ($Re = 364.52$, $We = 1.31$), (C) REGION 3 ($Re = 486.26$, $We = 5.71$) AND (D) REGION 4 ($Re = 652.63$, $We = 8.31$)

TABLE 5: SUMMARY OF NARX RESULT FOR ACCELERATION PREDICTION.

Region	Relative Error		Absolute Error	
	Testing	Training	Testing	Training
Region 1	4.85	4.71	0.0325	0.0330
Region 2	3.97	5.72	0.0158	0.0180
Region 3	3.09	3.53	0.0016	0.0124
Region 4	3.52	4.21	0.0121	0.0122
Mean	3.43%	4.11%		

magnitude. The prediction errors of a_c^* are summarized in Table 5 and are larger than those of the droplet shape. The reason is that the errors of the drop-deformation model will propagate into the drop-acceleration model. In contrast to the shape prediction, Region 4 has the best accuracy in acceleration prediction while Region 1 has the worst. This can be explained by the fact that the acceleration magnitudes of Region 1 varies in a wider range, compared to Region 4 (see Fig. 7). Even with these limitations, the largest relative error of any of the cases is 9.18%, which is associated with the $Re = 990.90$, $We = 1.98$ simulation case.

4. CONCLUSION

The shape deformation and acceleration of a free drop for different Re and We are simulated using 2D-axisymmetric interface-resolved simulations. In this regime, the drop shape can deviate significantly from the spherical shape but will not break. The drop shape evolution is characterized by the spherical harmonic modes. As expected, the $n = 2$ mode is the dominant mode, and the frequencies of all examined modes agree well with the Lamb frequencies. The frequency spectra of the mode coefficients show non-linear mode coupling for drops with high We , which is attributed to the large amplitude of deformation/oscillation.

Subsequently, the time-evolutions of the mode coefficients and drop acceleration are utilized to develop data-driven models for predicting the drop deformation and acceleration. The non-linear auto-regressive with exogenous input neural network (NARXNN) method is used for this purpose. Separate models are developed for drop deformation and acceleration in different regions of the Re - We parameter space. The models are first trained using the training data (92 cases) and then tested against the simulation results for the testing set (10 cases). Remarkably, the predictions and simulation results exhibit excellent agreement, particularly for shape prediction when $We \leq 6.5$. The developed models accurately predict the drop shape and acceleration with less than 6% and 10% relative error, respectively. In the present models, the results for the first few time steps up to the lag are used as inputs. In future research, we plan to acquire this initial data by utilizing methods such as singular value decomposition and kriging interpolation.

5. ACKNOWLEDGEMENTS

This research is supported by the ACS Petroleum Research Fund (#62481-ND9) and the NSF (#1942324). The Baylor High Performance and Research Computing Services (HPRCS) have been used for the present simulations.

REFERENCES

- [1] Lefebvre, A. H., and McDonell, V. G., 2017. *Atomization and sprays*. CRC press.
- [2] Ranger, A. A., and Nicholls, J. A., 1969. "Aerodynamic shattering of liquid drops.". *AIAA J.*, **7**, pp. 285–290.
- [3] Hsiang, L.-P., and Faeth, G. M., 1992. "Near-limit drop deformation and secondary breakup". *Int. J. Multiphase Flow*, **18**, pp. 635–652.
- [4] Meng, J. C., and Colonius, T., 2018. "Numerical simulation of the aerobreakup of a water droplet". *J. Fluid Mech.*, **835**, pp. 1108–1135.
- [5] Hsiang, L.-P., and Faeth, G. M., 1995. "Drop deformation and breakup due to shock wave and steady disturbances". *Int. J. Multiphase Flow*, **21**, pp. 545–560.
- [6] Rayleigh, L., 1879. "On the capillary phenomena of jets". *Proc. R. Soc. Lond.*, **29**, pp. 71–97.
- [7] Lamb, H., 1932. *Hydrodynamics*. Cambridge University Press.
- [8] Reid, W. H., 1960. "The oscillations of a viscous liquid drop". *Q. Appl. Maths.*, **18**, pp. 86–89.
- [9] Miller, C. A., and Scriven, L. E., 1968. "The oscillations of a fluid droplet immersed in another fluid". *J. Fluid Mech.*, **32**, pp. 417–435.
- [10] Prosperetti, A., 1980. "Normal-mode analysis for the oscillations of a viscous-liquid drop in an immiscible liquid". *J. Mecanique*, **19**, pp. 149–182.
- [11] Tsamopoulos, J. A., and Brown, R. A., 1983. "Nonlinear oscillations of inviscid drops and bubbles". *J. Fluid Mech.*, **127**, pp. 519–537.
- [12] Basaran, O. A., 1992. "Nonlinear oscillations of viscous liquid drops". *J. Fluid Mech.*, **241**, pp. 169–198.
- [13] Bergeles, K., Hardalupas, Y., and Taylor, A. M. K. P., 2018. "On the transient flow inside and around a deforming millimetre class oil droplet falling under the action of gravity in stagnant air". *Phys. Fluids*, **30**, p. 013305.
- [14] Lalanne, B., Tanguy, S., and Risso, F., 2013. "Effect of rising motion on the damped shape oscillations of drops and bubbles". *Phys. Fluids*, **25**, p. 112107.
- [15] Zhang, B., Ling, Y., Tsai, P.-H., Wang, A.-B., Popinet, S., and Zaleski, S., 2019. "Short-term oscillation and falling dynamics for a water drop dripping in quiescent air". *Phys. Rev. Fluids*, **4**, p. 123604.
- [16] Apte, S., Gorokhovski, M., and Moin, P., 2003. "LES of atomizing spray with stochastic modeling of secondary breakup". *Int. J. Multiphase Flow*, **29**, pp. 1503–1522.
- [17] Pai, M. G., and Subramaniam, S., 2006. "Modeling interphase turbulent kinetic energy transfer in lagrangian-eulerian spray computations". *Atomization Spray*, **16**, pp. 807–826.
- [18] Balachandar, S., 2009. "A scaling analysis for point particle approaches to turbulent multiphase flows". *Int. J. Multiphase Flow*, **35**, pp. 801–810.
- [19] O'Rourke, P. J., and Amsden, A. A., 1987. The tab method for numerical calculation of spray droplet breakup. Tech. Rep. Tech. Rep. LA-UR-2105., Los Alamos National Laboratory.
- [20] Maxey, M. R., and Riley, J. J., 1983. "Equation of motion for a small rigid sphere in a nonuniform flow". *Phys. Fluids*, **26**, pp. 883–889.
- [21] Kulkarni, V., Guildenbecher, D. R., and Sojka, P. E., 2012. "Secondary atomization of newtonian liquids in the bag breakup regime: Comparison of model predictions to experimental data". In ICLASS 2012, 12th International Conference on Liquid Atomization and Spray Systems.
- [22] Rimbart, N., Escobar, S. C., Meignen, R., Hadj-Achour, M., and Gradeck, M., 2020. "Spheroidal droplet deformation, oscillation and breakup in uniform outer flow". *J. Fluid Mech.*, **904**, p. A15.
- [23] Jackiw, I. M., and Ashgriz, N., 2021. "On aerodynamic droplet breakup". *J. Fluid Mech.*, **913**, p. A33.
- [24] Wan, Z. Y., Karnakov, P., Koumoutsakos, P., and Sapsis, T. P., 2020. "Bubbles in turbulent flows: Data-driven, kinematic models with history terms". *International Journal of Multiphase Flow*, **129**, p. 103286.
- [25] Zhang, J., Zhang, S., Zhang, J., and Wang, Z., 2021. "Machine learning model of dimensionless numbers to predict flow patterns and droplet characteristics for two-phase digital flows". *Applied Sciences*, **11**(9), p. 4251.
- [26] Andalib, S., Taira, K., and Kavehpour, H. P., 2021. "Data-driven time-dependent state estimation for interfacial fluid mechanics in evaporating droplets". *Scientific Reports*, **11**(1), p. 13579.
- [27] Yoon, I., Chergui, J., Juric, D., and Shin, S., 2022. "Maximum spreading of droplet-particle collision covering a low weber number regime and data-driven prediction model". *Physics of Fluids*, **34**(10), p. 102109.
- [28] Arrufat, T., Cialesi-Esposito, M., Fuster, D., Ling, Y., Malan, L., Pal, S., Scardovelli, R., Tryggvason, G., and Zaleski, S., 2020. "A momentum-conserving, consistent, volume-of-fluid method for incompressible flow on staggered grids". *Comput. Fluids*, **215**, p. 104785.
- [29] Zhang, B., Popinet, S., and Ling, Y., 2020. "Modeling and detailed numerical simulation of the primary breakup of a gasoline surrogate jet under non-evaporative operating conditions". *Int. J. Multiphase Flow*, **130**, p. 103362.
- [30] Popinet, S., 2009. "An accurate adaptive solver for surface-tension-driven interfacial flows". *J. Comput. Phys.*, **228**(16), pp. 5838–5866.
- [31] van Hooft, J. A., Popinet, S., van Heerwaarden, C. C., van der Linden, S. J. A., de Roode, S. R., and van de Wiel, B. J. H., 2018. "Towards adaptive grids for atmospheric boundary-layer simulations". *Bound.-Layer Meteor.*, **167**, pp. 421–443.
- [32] Becker, E., Hiller, W. J., and Kowalewski, T. A., 1991. "Experimental and theoretical investigation of large-amplitude oscillations of liquid droplets". *J. Fluid Mech.*, **231**, pp. 189–210.
- [33] Zhang, B., and Ling, Y., 2019. "High-fidelity modeling and simulation of primary breakup for a gasoline surrogate jet". In Proc. ICLASS-Americas 30th Annual Conference on Liquid Atomization and Spray Systems 30th Annual Conference on Liquid Atomization and Spray Systems.

[34] Menezes Jr, J. M. P., and Barreto, G. A., 2008. “Long-term time series prediction with the narx network: An empirical

evaluation”. *Neurocomputing*, **71**(16-18), pp. 3335–3343.